UCLA
Adaptive Optics for Extremely Large Telescopes 4 – Conference Proceedings

Title

Anti-aliasing wave-front reconstruction with Shack-Hartmann sensors

Authors

Bond, Charlotte
Fusco, Thierry
Correia, Carlos
et al.

Peer reviewed

Anti-aliasing wave-front reconstruction with Shack-Hartmann sensors

C. Z. Bond[a], C. Correia[a], J. Teixeira[b], J. F. Sauvage[a,b], J. P. Véran[c], and T. Fusco[a,b]

[a]Aix Marseille Université, CNRS, Laboratoire d'Astrophysique de Marseille, UMR 7326, 13388, Marseille, France
[b]ONERA, Optics department, 29 avenue de la Division Leclerc, 92322 Châtillon, France
[c]National Research Council Canada, CNRC

ABSTRACT

The discrete sampling of a wave-front using a Shack-Hartmann sensor limits the maximum spatial frequency we can measure and impacts sensitivity to frequencies at the high end of the correction band due to aliasing. Here we present Wiener filters for wave-front reconstruction in the spatial-frequency domain, ideally suited for systems with a high number of degrees of freedom. We develop a theoretical anti-aliasing (AA) Wiener filter that optimally takes into account high-order wave-front terms folded in-band during the sensing (i.e., discrete sampling) process. We present Monte-Carlo simulation results for residual wave- fronts and propagated noise and compare to standard reconstruction techniques (in the spatial domain). To cope with finite telescope aperture we've developed and optimised a Gerchberg-Saxton like iterative-algorithm that provides superior performance.

1. INTRODUCTION

The use of a Shack-Hartmann wave-front sensor to measure phase distortions introduces errors to the reconstructed phase due to the measurement process. It is our aim to develop reconstruction methods which utilise knowledge of how these measurement errors propagate through the system to reduce these errors. In this specific case we consider aliasing errors, an artefact of the discrete sampling of the wavefront.

Any discrete measurement cannot measure frequencies above the Nyqvist frequency $f_{\mathrm{Nyq.}} = \frac{f_{\mathrm{samp.}}}{2}$, where $f_{samp.}$ is the sampling frequency. In the case of wave-front measurements there exist spatial frequencies greater than $f_{\mathrm{Nyq.}}$ in the wave-front. These higher spatial frequencies can appear in the measurement as low spatial frequencies. This is the aliasing process, illustrated in figure 1 where for a given sampling frequency a high and low frequency signal yield the same measurement. Aliasing can affect any discrete measurement which contains frequencies above the Nyqvist frequency. The impact of aliasing on the measurement will depend on the system, i.e. how the aliasing errors propagate through the measurement process.

In the case of Adaptive Optics (AO) systems, aliasing errors occur during the measurement of the wave-front. In this case we consider spatial aliasing, in which the Nyqvist frequency is determined by the spatial sampling of the wavefront. With a classic wave-front sensor (WFS), the Shack-Hartmann (SH), this sampling is determined by the lenslet spacing. A SH-WFS is particularly susceptible to aliasing due to its performance as a slope sensor: it is more sensitive to higher spatial frequencies. Frequencies higher then $f_{\mathrm{Nyq.}}$ fold into the measurement and cause large errors in the estimation of the wavefront at spatial frequencies at the high end of the correctable band. The result is an over estimate of particular spatial frequencies in the wave-front and an inability to provide AO corrections up to the limits of the system (the number of modes correctable by the deformable mirror).

Here we present a solution to the aliasing problem: an anti-aliasing filter for wave-front reconstruction in the Fourier domain. Working in the Fourier domain allows the use of the Fast Fourier Transform (FFT) which offers significant reduction in computing time for high degree of freedom systems (computing time $\propto n \log(n)$ instead of $\propto n^2$). This will be the case for future Extremely Large Telescopes (ELTs) which will use a high number of correctable modes, significantly increasing the size of the control matrices. In addition the issue of aliasing is

Corresponding author: C. Z. Bond
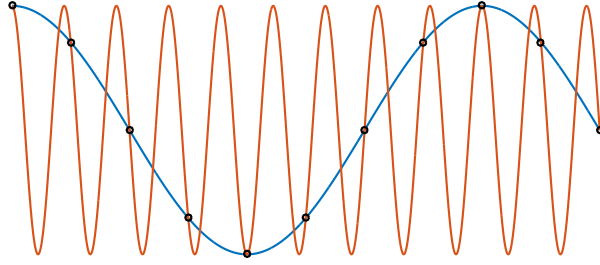E-mail: charlotte.bond@lam.fr

Figure 1. Illustration of aliasing. Two different waves are shown, a low frequency (blue) and high frequency (red) wave. For a specific sampling frequency (black circles) we can effectively measure the low frequency wave but the high frequency wave produces the same measurements. Hence the high frequency wave is an alias of the low frequency wave in such a measurement.

inherently a problem of spatial frequencies, which makes this the natural domain to approach the problem. Such a solution will be of particular interest for systems with no spatial filter, such as the HARMONI high contrast path in the European Extremely Large Telescope (E-ELT).

2. CONSTRUCTION OF THEORETICAL FILTERS

2.1 The forward model

The Shack-Hartmann sensor is inherently a slope measuring device. In the spatial domain (or direct space) the relationship between the measured slopes and the phase is given by:

$$s(\mathbf{x}) = \mathbf{G}\phi(\mathbf{x}) + \mathbf{n}(\mathbf{x}) \tag{1}$$

where s is the slope measurement, $\mathbf{x}$ is the spatial coordinate vector, G is the phase-to-slopes operator, ϕ is the phase, or wavefront, and n is the noise associated with the measurement. G describes the process by which the Shack-Hartmann measures the slope of the phase of the incident light. The reconstruction of the phase involves the inversion of G.

In direct space G can be modelled as a continuous function by a series of convolutions, as described in:[1]

$$G = \mathbf{III}\left(\frac{\mathbf{x}}{d}\right) \times \left[\Pi\left(\frac{\mathbf{x} - \frac{1}{2}}{d}\right) \otimes \Pi\left(\frac{\mathbf{x}}{\mathbf{v}T_s}\right) \otimes \bigtriangledown\right] \tag{2}$$

Here the gradient operator $\bigtriangledown$ represents the measurement of the slope. The comb function ($\mathbf{III}$) represents the discrete sampling of the wave-front, with d the lenslet separation. The convolutions ($\otimes$) with the two square functions (Π) represent the averaging process of the measurement, where the discrete measurement takes the average wave-front across the lenslet (spatial averaging) and across the measurement period (temporal averaging). This measurement is a series of convolutions, which can be expressed as simple multiplications in Fourier space. Therefore, we can go directly to the Fourier representation:

$$\tilde{s}(\kappa) = \tilde{\mathbf{G}}\tilde{\phi}(\kappa) + \tilde{\mathbf{n}}(\kappa) \tag{3}$$

where $\tilde{a}$ denotes the Fourier transform of a. If we can reconstruct in the Fourier domain to get $\tilde{\phi}$, using $\tilde{s}$ the Fourier transform of the original slope measurement, we simply use the inverse Fourier transform to get ϕ.

In direct space the reconstruction of the phase is achieved using the minimum mean square error (MMSE) method. In the Fourier domain this method is equivalent to a Weiner filter applied to the slopes in the Fourier domain:

$$\tilde{\phi} = \tilde{R}_x \tilde{S}_x + \tilde{R}_y \tilde{S}_y \tag{4}$$

where $\tilde{R}_x$ and $\tilde{R}_y$ are a Weiner filter with the general form:

$$\tilde{R}_x = \frac{\tilde{G}_x^*}{|\tilde{G}_x|^2 + |\tilde{G}_y|^2 + \gamma \frac{W_n}{W_\phi}} \quad \tilde{R}_y = \frac{\tilde{G}_y^*}{|\tilde{G}_x|^2 + |\tilde{G}_y|^2 + \gamma \frac{W_n}{W_\phi}} \tag{5}$$

The term $\gamma \frac{W_n}{W_\phi}$ is inversely proportional to the signal to noise ratio and avoids reconstructing to fit to the noise of the system, instead adhering to the MMSE condition of minimising the time-averaged, pupil integrated residual variance within the correctable band. W_n and W_ϕ are the power spectral densities (PSDs) of the noise and phase and γ is a constant, allowing us to tune the amplitude of this term to account for un-modelled system parameters. In the cases considered here the noise is assumed to be white noise.

2.2 Aliasing in the Fourier domain

Using the forward model in the Fourier domain the aliasing is traced through the system and the aliasing term identified, as shown in.[1] Figure 2 illustrates how higher frequency terms fold into the correctable band. The true PSD of the phase follows a $k^{-11/3}$ relationship. The dashed red curves in the figure illustrate the high terms folded into the measurement. The final measurement will be the sum of the true curve (the green curve) and the aliasing component (the red dashed curve). This is illustrated in figure 3, showing plots of the PSD of the expected phase with and without aliasing. For the most part the curves are very similar. At the high end of the correctable band there is a significant difference between the two PSDs: aliasing in the measurement results, on average, in an over-estimation of the power in the high spatial frequencies.

The idea of producing an anti-aliasing filter is to assess the performance of a post-facto aliasing mitigation reconstructor when no optical spatial filtering can be implemented within the system, or where $\frac{d}{r_0}$ (the ratio of the lenslet spacing to the Fried parameter) is too large for such filtering to be effective. The MMSE minimisation, with an extended forward model, leads to a solution that is structurally similar to the previous filters with an extra term accounting for the aliasing PSD (computed in[1]):

$$\tilde{R}_x = \frac{\tilde{G}_x^*}{|\tilde{G}_x|^2 + |\tilde{G}_y|^2 + \gamma_a \frac{W_a}{W_\phi} + \gamma_n \frac{W_n}{W_\phi}} \quad \tilde{R}_y = \frac{\tilde{G}_y^*}{|\tilde{G}_x|^2 + |\tilde{G}_y|^2 + \gamma_a \frac{W_a}{W_\phi} + \gamma_n \frac{W_n}{W_\phi}} \tag{6}$$
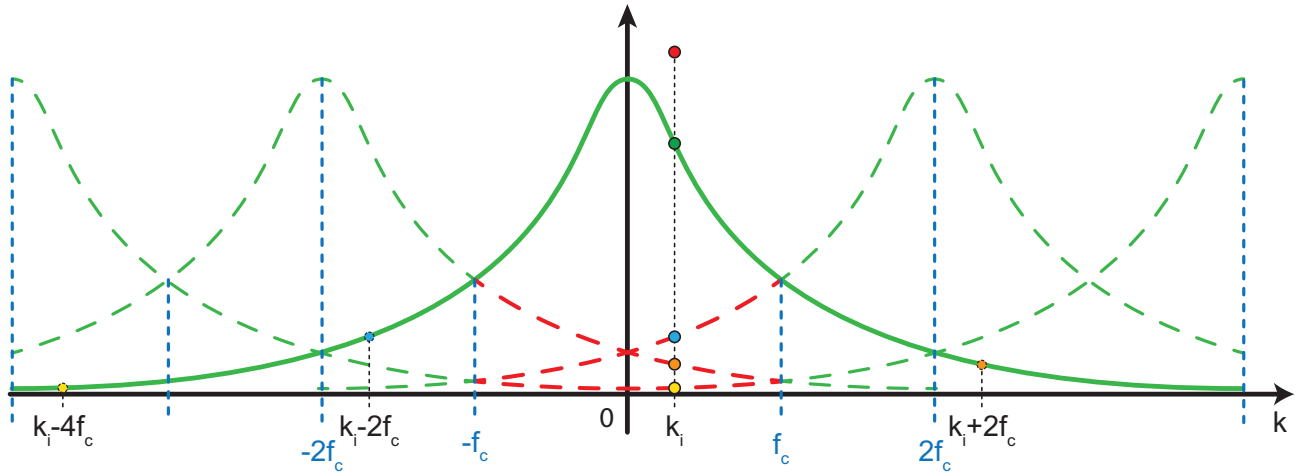

Figure 2. Illustration of aliasing in the Fourier domain. The solid green line shows the power spectral density (PSD) of the different spatial frequencies present in the wave-front. f_c is the cut-off frequency (or Nyqvist frequency) the maximum measurable frequency and, in a SH AO system, the end of the correctable band. Frequencies $> f_c$ will fold into the measurement as aliases of the in-band frequencies. This folding in is illustrated by the dashed red lines, with the dashed green showing reflections of the original PSD which follow the folded frequencies.
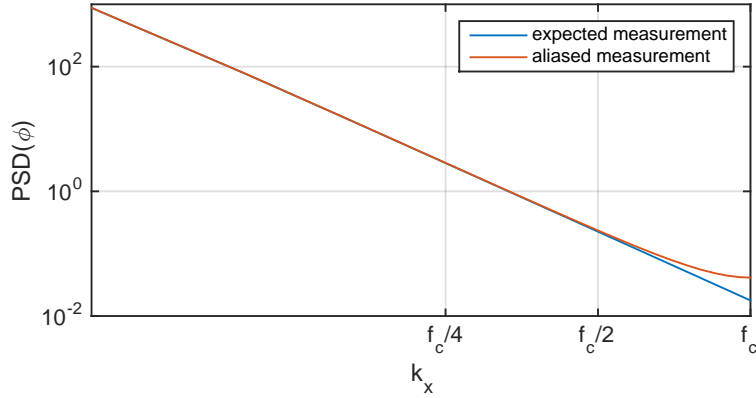
Figure 3. Power spectral densities (PSDs) of the phase with and without aliasing errors. The expected measurement follows a $k^{-11}3$ trend. The two curves are very similar at low spatial frequency but at the high end of the correctable band, close to the cut-off frequency f_c, the impact of aliasing causes a significant difference in expected PSD.

Here the term $\gamma_a \frac{W_a}{W_\phi}$ acts to compensate the impact of aliasing in the measurement process. W_a is the PSD of the aliased component of the slopes, W_ϕ is the PSD of the phase and γ_a is a coefficient we will tune in practice. The implementation of such a filter should avoid the over-estimation of frequencies at the high end of the band due to aliasing.

2.3 Fourier filters

The overall form of the filter depends on the formation of the phase-to-slopes operator G. The forward model presented above, is based on a continuous model in direct space, using the continuous gradient operator $\bigtriangledown$. This yields a filter we refer to as the *Rigaut* filter, without the inclusion of aliasing, and the *Anti-aliasing* filter when this term is included. Additional sensor models, based on discrete first differences as approximations of the spatially averaged gradient, have previously been proposed and their filters derived.[2] The different models account for different sensor geometries: the point at which the phase differences are calculated. 3 such sensor geometries are illustrated in figure 4:
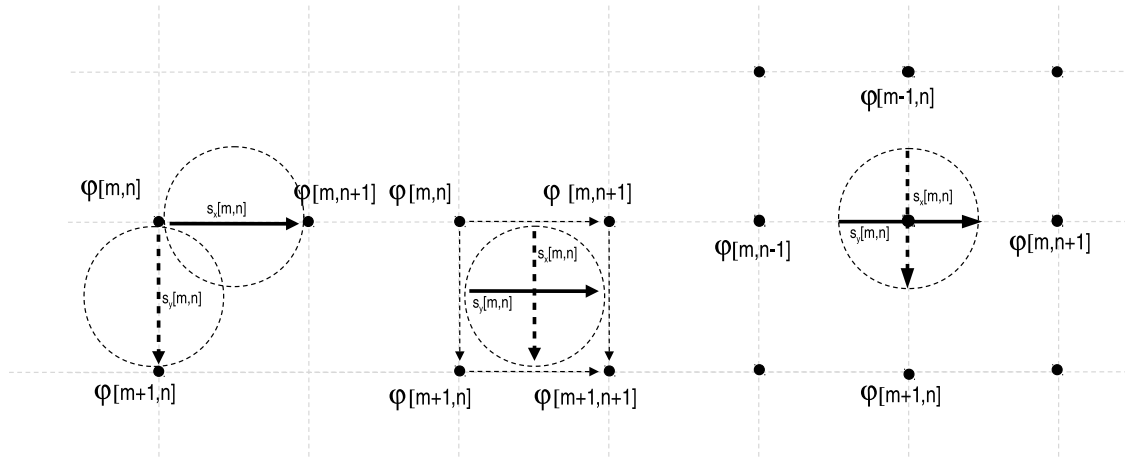

Figure 4. Diagrams showing different possible geometries used to describe the slopes measurements. In each case the solid arrow represents the discrete measurement of the x slope and the dashed arrow represents the y slope, with the solid points as the actuator positions. From left to right we have the Hudgin geometry, the Fried geometry and the Southwell geometry.

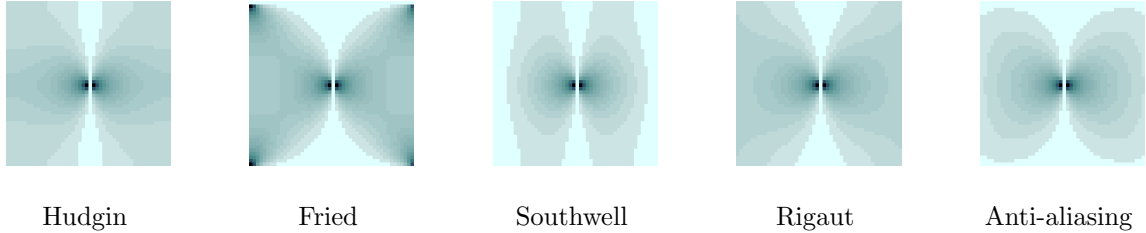| Hudgin | Fried | Southwell | Rigaut | Anti-aliasing |

Figure 5. Plots of different filters for wave-front reconstruction in the Fourier domain. The Hudgin, Fried and Southwell filters originate from modelling the system using different lenslet geometries. The Rigaut filter is the result of a continuous approach using the forward model, with the anti-aliasing filter an extension of the Rigaut filter to include aliasing errors. In each case the x filter is shown and the centre of each image corresponds to $k_x = 0$, $k_y = 0$.

- **Hudgin geometry**: Takes the first difference across two adjacent phase points.

- **Fried geometry**: Corresponds to the geometry of the SH in which the measurement includes an averaging across the edges of the sub-aperture, i.e. the first difference between the average of two adjacent points.

- **Southwell geometry**: Assumes the measurement point lies at the intersection of the grid, exactly at the point of reconstruction.

All three models can be used to construct Fourier filters, with the addition of small shifts in the case of the Hudgin and Southwell filters, to correlate them with the SH geometry. Each filter has specific features. For example, using a non-Fried geometry can be an advantage as it avoids the particular susceptibility of this geometry to the waffle frequency, $k = \frac{1}{2d}$, where d is the lenslet spacing. The advantage of using such models over the more complete Rigaut filter is that they produce closed-form solutions when adapting to the annular telescope pupil.[3] In addition, modelling in the spatial-frequency domain provides straightforward results for noise and aliasing propagation and the overall residual signal.

Figure 5 shows plots of the 5 filters: Hudgin, Fried, Southwell, Rigaut and Anti-aliasing. At the centre of the plots (where spatial frequencies k_x and k_y are low) the filters appear similar, whilst at the edges (high frequencies) we observe very different features. For example the Fried filter exhibits a strong response close to the waffle frequency (towards the corners) as this geometry is insensitive to waffle. The waffle frequency itself is set to zero to avoid a pole here.[4] In the context of this paper we are most interested in the differences between the Rigaut and Anti-aliasing filters. In the Anti-aliasing filters the higher frequencies are tailored off to avoid over-estimation caused by aliasing in the measurement.

The use of any of these filters assumes knowledge about our system. One possible method to produce a filter which matches the intrinsic behaviour of the wave-front sensor and deformable mirror (DM) interaction is to measure the filter by 'poking' the DM. In this case the DM is fed with the Fourier modes and $\tilde{G}$ is the measured response to these modes. A filter using this measured $\tilde{G}$ will directly encode the sensitivity of the system to a specific frequency.[5]

3. END-TO-END SIMULATIONS

To test the improvement offered by these filters in a real system they were implemented in end-to-end simulations of realistic adaptive optics systems. We use the simulation code OOMAO[6] (Object-Oriented Matlab Adaptive Optics toolbox) to model a telescope and AO system. In the process of this investigation we developed a series of Matlab functions for the implementation of Fourier wave-front reconstruction with OOMAO, which will shortly be available with the latest OOMAO library. These functions take the form of the Matlab class `fourierReconstructor`. Using these tools we were able to test the performance of our Anti-aliasing filter against the Rigaut filter and a direct space MMSE reconstruction method, comparing performance in terms of strehl ratio and residual phase PSD. The parameters used in these simulations are summarised in table 1.

Table 1. Summary of the key simulation parameters for the end-to-end simulation results presented here. r_0 is the Fried parameter, L_0 is the outer scale, F_s is the temporal sampling of the wavefront and f_c is the cut-off spatial frequency. DM coupling refers to the overshoot of an individual actuators influence function on its neighbours.

Parameter	Value
r_0	$15.5\,\mathrm{cm}$
L_0	$25\,\mathrm{m}$
No. of lenslets	40
No. of pixels	240
Telescope diameter	$8\,\mathrm{m}$
DM coulpling	35%
F_s	$1\,\mathrm{kHz}$
f_c	$2.5\,\mathrm{m}^{-1}$

3.1 Dealing with finite apertures

In order to implement this Fourier approach on realistic data we need to deal with the impact of the finite aperture of the telescope. The Fourier transform is a transform of a cartesian coordinate system, not a cylindrical system. The telescope aperture effectively cuts off any data outside the pupil and results in a sharp change in the data. This effect will appear in the Fourier transform as spurious high frequency terms as the decomposition attempts to represent this sharp change. To avoid such an error the data inside the aperture must be numerically extended to fill the cartesian grid. In addition the data must fulfil periodic conditions in order for us to apply the Discrete Fourier Transform (DFT) on discrete data.

There are many ways in which the slopes can be extended. We have investigated several different methods and assessed their impact on the performance of the reconstruction, of which several are illustrated in figure 6. For example, the Hudgin extension simply takes the last valid data point and extends it along y for the x slopes and along x for the y slopes. A more complex example is based on a Gerchberg-Saxton algorithm,[3, 7, 8] in which the original slopes data is propagated through the reconstruction process to get a temporary $\tilde{\phi}$. The operator $\tilde{G}$ is then applied to $\tilde{\phi}$ to get the temporary Fourier slopes $\tilde{s}$. Applying the inverse Fourier transform we get s, slopes in direct space which are now extended outside the aperture. The data within the original aperture region is replaced by the original slope data. This process is illustrated in the right panel of figure 6. In general several iterations of this process are required.

In practice we have found the Gerchberg method produces the best results, although the other methods are satisfactory and avoid a large number of iterations. The extension of the slopes is a crucial step in order to reconstruct in the Fourier domain and failure to carry out this process will have a large impact on the performance.

3.2 Initial numerical tests

The first test of the anti-aliasing method is to check that the measurement of the PSD in a realistic simulation corresponds to that predicted by the theory. Figure 7 shows the results of such a test: the theoretical and simulated PSDs of the slopes are compared for different x and y spatial frequencies. The results are in good agreement, with the analytic form including the aliasing term calculated through the forward model.

3.3 Open loop simulations

Firstly we consider an open loop AO system. The simulation was setup with the parameters specified in table 1. The loop was simulated for a variety of different Fourier filters and using a direct space MMSE method for comparison. In this case we are concerned with the performance of the Anti-aliasing filter compared to the Rigaut filter. Here we present preliminary results using the Anti-aliasing and Rigaut filters. An optimal aliasing coefficient of $\gamma = \pm 0.2$ is used throughout.
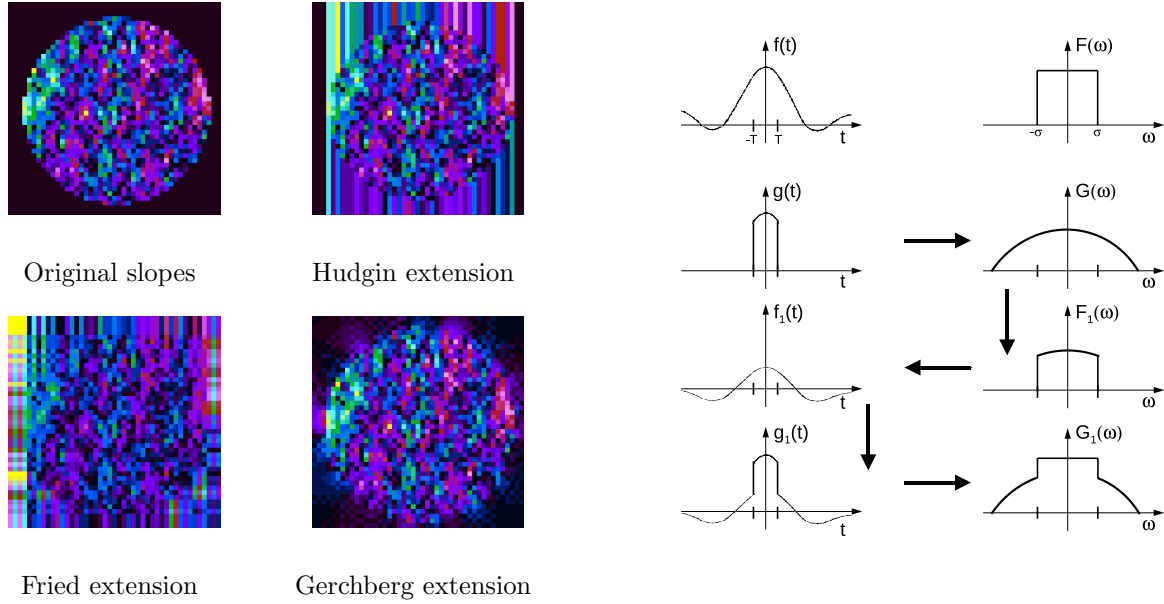
Original slopes   Hudgin extension

Fried extension   Gerchberg extension

Figure 6. Plots illustrating the extension of the slope data outside the telescope aperture. **Left**: 3 examples of different extension methods, showing the original slopes, the Hudgin extended slopes, the Fried extended slopes and the Gerchberg extended slopes. **Right**: Illustrations showing the Gerchberg extension method. A continuous function $f(t)$, with Fourier transform $F(\omega)$, is sampled over a finite period to give a function $g(t)$. The Fourier transform of the discrete function is taken $(G(\omega))$ and truncated by a given bandwidth $(F_1(\omega))$. The inverse transform is taken to get $f_2(t)$, with data now filling an extended period. The data across the original sample period replaces the data across the same period in f_2, giving an extended version of our original function $(g_1(t))$. Multiple iterations of this method cause the function to tend to the original continuous function.
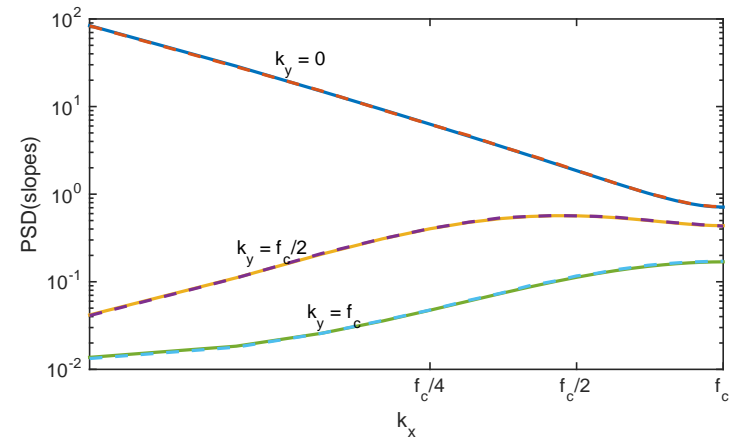

Figure 7. Analytical (solid lines) and numerical (dashed lines) results for the power spectral density (PSD) of the slopes measured by a Shack-Hartmann wave-front sensor. The PSD is shown over the x spatial frequency with different slices in the y spatial frequency. The analytic equations include aliasing errors.

The figures of merit we consider in this investigation are the residual phase PSD and the Strehl ratio in K-band. In figure 8 plots of the residual phase PSD are shown across a range of spatial frequencies. The PSDs shown here correspond to the original uncorrected phase, and the residual using the Rigaut filter and Anti-aliasing filters with $\gamma = \pm 0.2$. For each filter the reconstruction provides corrections within the correctable band, with a cut-off frequency (last correctable frequency) of $f_c = 2.5\,\text{m}^{-1}$. This also corresponds to the waffle

frequency.

The 3 filters exhibit very similar performance over the low end of the correction band, as is expected, as this region is relatively unaffected by aliasing. The plot in the right panel of figure 8 shows a zoom across the high end of the band, where we begin to observe differences between the different filters. The positive Anti-aliasing filter ($\gamma = 0.2$) provides better performance than the Rigaut filter over most of the high frequencies (the residual phase is lower), whilst the negative Anti-aliasing filter ($\gamma = -0.2$) performs worse over this range.

Residual phase PSD   Zoom in on residual phase PSD
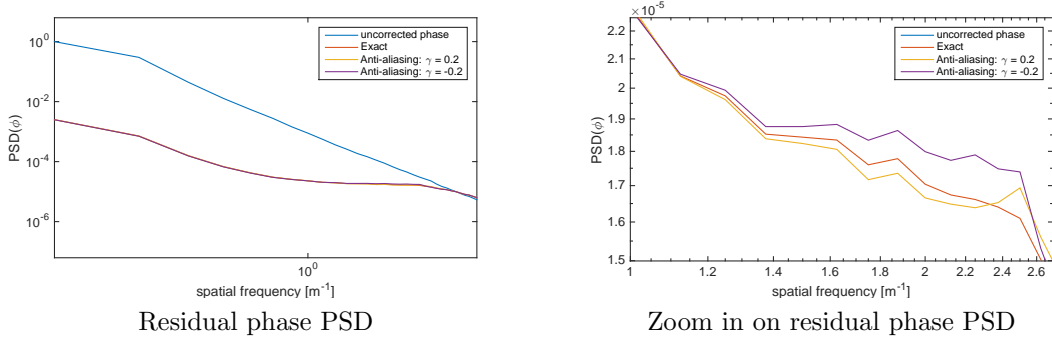
Figure 8. Power spectral densities (PSDs) of the uncorrected phase and residual phase for different Fourier reconstructors, the Rigaut filter and an Anti-aliasing filter with positive and negative aliasing coefficients. The left panel shows a range of frequencies across the correctable band. The right panel shows a close up of the high end of the correctable band ($f_c = 2.5\,\mathrm{m}^{-1}$).

To get a better understanding of the performance of the Anti-aliasing filter compared to the Rigaut the fractional difference between the residuals were calculated. This is shown in figure 9, for both the positive and negative Anti-aliasing filters. The negative regions indicate a better performance using the Anti-aliasing filter over the Rigaut, in terms of residual phase. These plots show that both the positive and negative Anti-aliasing filter provide greater correction than the Rigaut at certain spatial frequencies. These results are promising as they illustrate an ability to perform better across the whole correctable band. However, we would expect the positive filter to provide such a performance, with the negative filter performing worse over the whole correctable band. This suggests we require further optimisation of the reconstruction process. This could be in the form of optimising the filters themselves or in reducing errors introduced in some of the additional steps, such as the extension of the slopes.

To analyse the overall performance of the different filters we consider the Sterol ratio for K-band. The results are summarised in table 2. Both Anti-aliasing filters perform slightly better than the Rigaut. Here we also show the impact of the choice of extension: there is a significant improvement in Strehl using the Rigaut filter when the Gerchberg extension is used instead of the simple Hudgin extension. This further motivates the the desire to further optimise the reconstruction process, focusing on the extension of the slopes in particular.

Table 2. Strehl ratio for different reconstruction methods within open loop end-to-end simulations. Results are shown for different Fourier reconstructors and a direct space MMSE method for comparison.

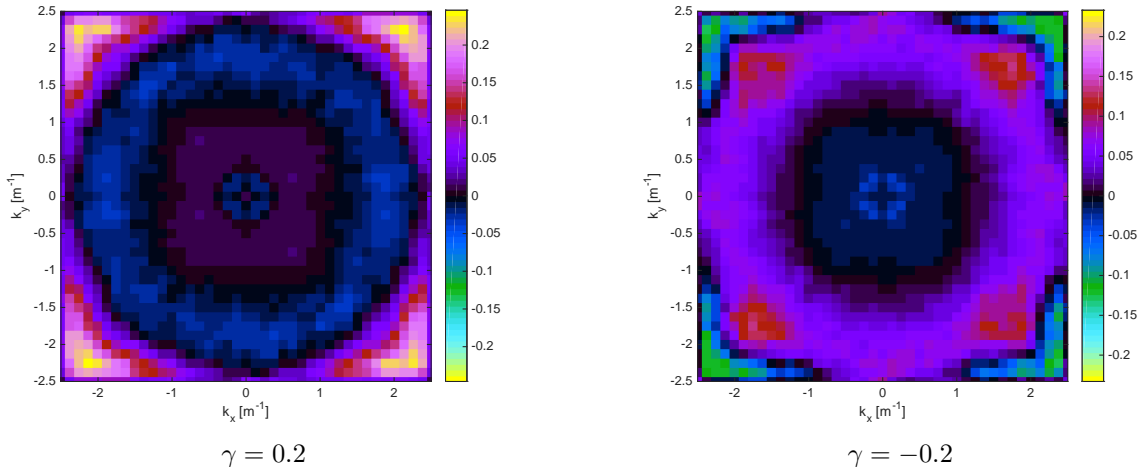| Reconstructor	Strehl (K-band)
MMSE (direct space)	96.7%
Rigaut (Gerchberg extension)	94.3%
Rigaut (Hudgin extension)	92.8%
Anti-aliasing ($\gamma = 0.2$)	94.5%
Anti-aliasing ($\gamma = -0.2$)	94.5%

$\gamma = 0.2$ $\gamma = -0.2$

Figure 9. Fractional difference between the residual phase PSDs for the Anti-aliasing and Rigaut filters, for positive and negative aliasing coefficients. Negative regions indicate a better performance with the Anti-aliasing filter, positive indicate the Rigaut provides the better results, in terms of minimising the residual phase.

3.4 Closed loop simulations and temporal filtering

Finally we present initial results from closed loop simulations, using an integrator with a 1 frame delay. The performance in terms of Strehl ratio is summarised in table 3. The Fourier filters perform well, matching the performance of the direct space MMSE. However, as the filters used here were developed for open loop, as opposed to closed loop, we do not observe a noticeable improvement when using the Anti-aliasing filter when compared to the Rigaut. A filter designed for closed loop should include the dynamics of the transfer function and one such filter is currently being developed.

Table 3. Strehl ratio for different reconstruction methods applied to close loop end-to-end simulations. The results are shown for two Fourier reconstructors and a direct space MMSE.

Reconstructor	Strehl (K-band)
MMSE (direct space)	94.4%
Rigaut (Gerchberg extension)	94.7%
Anti-aliasing ($\gamma = 0.2$)	94.6%

4. CONCLUSION AND OUTLOOK

Here we report progress on a Fourier filter designed to avoid errors due to aliasing in Shack-Hartmann measurements of the wave-front. Building on the theoretical derivation of this filter in[1] we have adapted these filters to end-to-end Monte Carlo simulations of adaptive optics systems. This has included the development of a Gerchberg-like process to extend the slope data beyond the aperture of the telescope, for compatibility with the Fourier transform. This method has provided superior performance to other extension methods, with the disadvantage of additional computations. These filters and the process of Fourier reconstruction has been included in OOMAO within the `fourierReconstructor` class, extending the functionality of OOMAO to include different Fourier reconstructors.

Initial results from full open and closed loop simulations yield promising results. The use of the Anti-aliasing filter provides some improvement, but not over all expected frequencies. However, the results using positive and negative aliasing coefficients suggest improvement over the whole correctable band is possible with further optimisation. Subsequent further tests have demonstrated greater performance with minor modifications to

the filters, which will be published shortly. Further analysis of the Gerchberg extension is required to identify any additional errors this process introduces to the data, and optimal performance may be achieved using a end-to-end measured filter in place of our analytic ones.

Finally the generalisation of closed loop PSD and PSF modelling using different possible controllers has been completed and will be applied to closed loop simulations for testing. In addition we will include wind-prediction and a coloured-noise state-space model.

ACKNOWLEDGMENTS

REFERENCES

[1] Correia, C. M. and Teixeira, J., "Anti-aliasing Wiener filtering for wave-front reconstruction in the spatial-frequency domain for high-order astronomical adaptive-optics systems," *Journal of the Optical Society of America A* **31**(12), 2763–2774 (2014).

[2] Freischlad, K. R. and Koliopoulos, C. L., "Modal estimation of a wave front from difference measurements using the discrete Fourier transform," *Journal of the Optical Society of America A* **3**(11), 1852–1861 (1986).

[3] Correia, C., Kulcsár, C., Conan, J.-M., and Raynaud, H.-F., "Hamann modelling in the discrete spatial-frequency domain: application to real-time reconstruction in adaptive optics," in [*SPIE 7015*], (2008).

[4] Poyneer, L. A., Gavel, D. T., and Brase, J. M., "Fast wave-front reconstruction in large adaptive optics systems with use of the Fourier transform," *Journal of the Optical Society of America A* **19**(10), 2100–2111 (2002).

[5] Poyneer, L. A. and Véran, J.-P., "Optimal modal Fourier-transform wavefront control," *Journal of the Optical Society of America A* **22**(8), 1515–1526 (2005).

[6] Conan, R. and Correia, C., "Object-oriented Matlab adaptive optics toolbox," in [*SPIE 9148*], (2014).

[7] Gerchberg, R. W., "Super-resolution through Error Energy Reduction," *Optica Acta* **21**(9), 709–720 (1974).

[8] Papoulis, A., "A new algorithm in spectral analysis and band-limited extrapolation," *IEEE Transactions on Circuits and Systems* **22**(9), 735–742 (1975).